

ACCEPTED MANUSCRIPT • OPEN ACCESS

Mapping and spectroscopy of telecom quantum emitters with confocal laser scanning microscopy

To cite this article before publication: Thomas Descamps *et al* 2024 *Nanotechnology* in press <https://doi.org/10.1088/1361-6528/ad5dbd>

Manuscript version: Accepted Manuscript

Accepted Manuscript is “the version of the article accepted for publication including all changes made as a result of the peer review process, and which may also include the addition to the article by IOP Publishing of a header, an article ID, a cover sheet and/or an ‘Accepted Manuscript’ watermark, but excluding any other editing, typesetting or other changes made by IOP Publishing and/or its licensors”

This Accepted Manuscript is © 2024 The Author(s). Published by IOP Publishing Ltd.



As the Version of Record of this article is going to be / has been published on a gold open access basis under a CC BY 4.0 licence, this Accepted Manuscript is available for reuse under a CC BY 4.0 licence immediately.

Everyone is permitted to use all or part of the original content in this article, provided that they adhere to all the terms of the licence <https://creativecommons.org/licenses/by/4.0>

Although reasonable endeavours have been taken to obtain all necessary permissions from third parties to include their copyrighted content within this article, their full citation and copyright line may not be present in this Accepted Manuscript version. Before using any content from this article, please refer to the Version of Record on IOPscience once published for full citation and copyright details, as permissions may be required. All third party content is fully copyright protected and is not published on a gold open access basis under a CC BY licence, unless that is specifically stated in the figure caption in the Version of Record.

View the [article online](#) for updates and enhancements.

Mapping and spectroscopy of telecom quantum emitters with confocal laser scanning microscopy

Thomas Descamps^{1*}, Alexandros Bampis¹, Maximilien Huet¹,
Mattias Hammar² and Val Zwiller^{1*}

¹ Department of Applied Physics, Royal Institute of Technology, Roslagstullsbacken 21, 10691 Stockholm, Sweden

² Department of Electrical Engineering, Royal Institute of Technology, 164 40 Kista, Sweden

* Corresponding authors: Thomas Descamps and Val Zwiller

Email: descamps@kth.se and zwiller@kth.se

Abstract. Efficiently coupling single-photon emitters in the telecommunication C-band that are not deterministically positioned to photonic structures requires both spatial and spectral mapping. This study introduces the photoluminescence mapping of telecom C-band self-assembled quantum dots (QDs) by confocal laser scanning microscopy, a technique previously unexplored in this wavelength range which fulfills these two requirements. We consider the effects of distortions inherent to any imaging system but largely disregarded in prior works to derive accurate coordinates from photoluminescence maps. We obtain a position uncertainty below 11 nm for 10% of the QDs when assuming no distortions, highlighting the potential of the scanning approach. After distortion correction, we found that the previously determined positions are on average shifted by 428 nm from the corrected positions, demonstrating the necessity of this correction for accurate positioning. Then, through error propagation, the position uncertainty for 10% of the QDs increases to 110 nm.

Keywords: quantum dot imaging, confocal laser scanning microscopy, single-photon source, telecom wavelength

1. Introduction

A shared fundamental requirement for two essential technologies in quantum information, namely quantum networks for secure communication [1, 2, 3] and on-chip photonic circuits for quantum computing [4, 5], is the need for single-photon emitters. Among various solid-state candidates, semiconductor quantum dots (QDs) emerge as a viable source of pure [6], indistinguishable [2, 7] single-photons as well as entangled photon pairs [1, 8]. While extensively studied with intrinsic emission wavelengths below 1 μm , ongoing efforts aim to extend their emission to the telecommunication O and C band to minimize losses in optical fibers [9]. Yet, the limited brightness of the sources originating from the long QD excitations lifetime and the total internal reflections

1
2
3
4
5
6
7
8
9
10
11
12
13
14
15
16
17
18
19
20
21
22
23
24
25
26
27
28
29
30
31
32
33
34
35
36
37
38
39
40
41
42
43
44
45
46
47
48
49
50
51
52
53
54
55
56
57
58
59
60

2

occurring at the surface of the semiconductor limit their direct use in scaled quantum technologies. These restrictions can be overcome by coupling the emitters to resonant photonic cavities fabricated in the semiconductor matrix [10, 11, 12], but deterministic integration is complicated by multiple factors. These include challenges related to the processing of the host material [13, 14] and fabrication imperfections that may cause deviations in the cavity shape, leading to a spectral mismatch between the cavity mode and the emitter [15] or limit the quality factor [15, 16]. In addition, surface defects created during nanofabrication can broaden the linewidth of the emitter and introduce spectral wandering [17] and random processes introduced by the growth process further complicate the integration. The latter issue first includes the random distribution of the QDs in the plane perpendicular to the growth direction. Second, fluctuations in their lateral sizes introduce uncertainties in their exact emission properties (emission wavelength and linewidth, fine structure splitting), which can be further exacerbated by local changes in strain and charge environment [18, 19, 20]. Consequently, spatial identification and spectral characterization of the QDs become two prerequisites for efficient coupling to the cavity mode. Various mapping techniques have been developed for this purpose: wide-field photoluminescence (PL) imaging [21, 22, 23], confocal PL scanning [24], in-situ photolithography [25] and in-situ electron beam lithography (EBL) [26]. While primarily applied to quantum dots emitting below 1 μm , these methods are typically a compromise between ease of mapping and processing, availability and final accuracy of the alignment. Their extension to emitters in the telecommunication O- and C- bands has become a technological necessity, but comes with more challenges. On the one hand, the QD excitations tend to be dimmer due to their longer lifetime, requiring longer exposure times. For neutral excitons generated by above-band excitations, previous studies reported lifetimes of approximately 1.29 ns for InAs QDs grown on a metamorphic buffer (MMB) [27] and 1.32 ns for InAs/InP QDs [28], both emitting in the C-band. In comparison, the decay time decreases to about 200 ps for GaAs QDs in nanoholes emitting around 795 nm [29, 30] and about 800 ps for InGaAs/GaAs emitting between 900 and 950 nm [18]. For trions, the lifetime is about 1.55 ns on average for InAs QDs on MMB [31], and about 2.6 ns for InAs/InP QDs [32], while remaining below 1 ns for InGaAs/GaAs QDs and GaAs in nanoholes [7, 18]. Under phonon-assisted two-photon excitation, the lifetimes of the exciton and biexciton for InAs QDs grown on MMB [33] were found to be 1.256 ns and 446 ps respectively, while 259 ps and 120 ps were measured for GaAs QDs in nanoholes [34]. On the other hand, commercial InGaAs cameras commonly used at these wavelengths, offer higher quantum efficiency but typically have lower resolution and suffer from higher electronic noise compared to Si cameras operating at shorter wavelengths. The dark current is larger by at least four orders of magnitude depending on the cooling temperature [35, 36], making the detection of low-intensity signals more challenging. Nonetheless, wide-field imaging of 1550 nm quantum dots has been recently demonstrated with a thermo-electrically cooled InGaAs camera [36].

Here, we present the PL mapping of telecom C-band QDs by confocal laser

scanning microscopy. In addition to obtaining the spatial coordinates of the emitter, the emission wavelength of the collected photons can be simultaneously determined by a spectrometer with a linear InGaAs photodiode array (PDA). When the full spectrum is not required, the signal can be filtered with a narrow bandpass filter and recorded with a superconducting nanowire single-photon detector (SNSPD), allowing a faster acquisition and an enhanced detection of weak emitters. Besides, we detail a numerical procedure to obtain the coordinates of the QDs from a recorded PL map. We also consider the distortion of the acquired maps, which can result from various imperfections in the scanning system. First, geometric deformations can arise if the optical beams do not impinge on the center of the scanning mirror [37]. Perspective distortion may also occur if the sample plane is not perfectly perpendicular to the objective optical axis [38], and barrel or pincushion distortions can be caused by an aperture within the optical system [38]. Distortions were largely overlooked by previous studies [36, 39, 40], assuming their impact was negligible. However, the QD positions found with the imaging system can be misleading, since even imperceptible distortions can significantly shift the actual positions of the QDs on the acquired maps. With our method applied on a moderately bright QD located within a 390x390 pixel photoluminescence map acquired over a 10.5-hour period, we obtain a positioning uncertainty below 15 nm when neglecting distortions. After distortion correction, we find that the previously determined position is shifted by 303 nm compared to the corrected QD position, underlining the need for distortion corrections. The positioning uncertainty then increases to about 155 nm after correction due to error propagation. For lower resolution maps (240x230 pixels), we find that 10% of the QDs can be located with an uncertainty of 11 nm and 110 nm before and after correction of distortions, respectively. On average, the image distortion introduced a 428 nm shift on the QD positions.

2. Materials and Methods

The sample investigated is grown by metal-organic vapor-phase epitaxy (MOVPE) on a Si-doped (100) GaAs substrate. The heterostructure consists of a 19.5 pairs of AlAs/GaAs (134.4 nm/ 114.6 nm) distributed Bragg reflector, a 1150 nm $\text{In}_x\text{Ga}_{1-x}\text{As}$ metamorphic buffer (MMB) layer with indium content gradually increased from $x = 0.015$ to $x = 0.4$, active InAs quantum dots and a 205 nm $\text{In}_{0.3}\text{Ga}_{0.7}\text{As}$ capping layer. The presence of the MMB layer relaxes the lattice strain on the quantum dots [33, 41], which increases their lateral size and shifts their emission wavelength to 1550 ± 20 nm. The QD density is estimated by atomic force microscopy on a similar uncapped sample to be approximately $3.9 \times 10^9 \text{ cm}^{-2}$, which corresponds to a mean QD separation of 160 nm. The average diameter for QDs with heights below 10 nm is 47 nm. A 5x5 grid made of Ti (5 nm) and Au (80 nm) is patterned on the surface by EBL and lift-off. The metal stripes are 3 μm wide and the pitch between two square unit cells is 23 μm .

As shown in Figure1(a), the sample is mounted on xyz nanopositioner stages inside a cryostat equipped with a fixed cryogenic objective ($NA = 0.77$). In our scanning

1
2
3
4
5 approach, the QDs are quasi-resonantly excited into the p-shell through the objective
6 with a pulsed laser at 1470 nm (80 MHz repetition rate) coupled to a single mode fiber.
7 The signal collected by the same objective is coupled to a second single mode fiber and
8 either directed to the spectrometer or to the SNSPD. With this confocal arrangement,
9 better spatial resolution can be obtained compared to the wide-field approach. The
10 excitation and detection beams can be deflected in steps by a dual-axis scanning mirror
11 with a high angular resolution ($22 \mu\text{rad}$) and good repeatability ($40 \mu\text{rad}$), allowing to
12 perform PL mapping. A scanning lens ($f = 50 \text{ mm}$) and a tube lens ($f = 150 \text{ mm}$) are
13 inserted between the scanning mirror and the objective to form a 4-f optical system.
14 The objective is designed to be apochromatic between 1170 and 1580 nm, and the
15 scanning and tube lenses are achromatic over the same wavelength range, but we limit
16 our mapping to the emission range of our QDs. In order to further minimize chromatic
17 aberrations, the QDs are excited quasi-resonantly. To simultaneously image the metal
18 grid, used as a reference for alignment, a fiber-coupled incoherent light source emitting
19 (LED at 1550 nm with 50 nm bandwidth) is added in the excitation path with a fiber
20 combiner. This configuration ensures that the spots of these two signals perfectly overlap
21 on the surface of the sample. After filtering the excitation laser with a long pass filter,
22 the detected signal then consists of the QD PL signal together with the incoherent light
23 reflected by the alignment marks and the surface. The choice of the emission wavelength
24 for the LED ensures that both the PL signal and the reflected incoherent light share
25 at the same focal point. By comparing the reflectance of gold with InGaAs at 1550
26 nm, the markers are expected to be approximately three times brighter than the bare
27 surface. The use of an incoherent light source is necessary to avoid diffraction patterns
28 at the edges of the grid, which simplifies its detection. We estimate the spot size to be
29 close to the Rayleigh diffraction limit. Assuming uniform illumination of the objective,
30 the resulting lateral resolution of the scanner is therefore $d = 0.61 \cdot \lambda/NA \approx 1.23\mu\text{m}$,
31 which is smaller than the width of the metal strips and ensures their identification. To
32 compare with our scanning-based imaging, a wide-field image of the surface can also
33 be obtained with an InGaAs SWIR camera (1280x1024 pixels chip) thermo-electrically
34 cooled to 10°C . The QDs are then off-resonantly excited with a 650 nm LED, and the
35 metal grid is imaged by reflection of 1550 nm light generated by a free-space LED. The
36 signal is filtered with a $(1550 \pm 6) \text{ nm}$ bandpass filter and then focused with a lens to
37 fill the camera sensor area with a x150 magnification.
38
39
40
41
42
43
44
45
46
47
48
49

50 **3. Results**

51 *3.1. Wavelength resolution*

52 One unit cell of the grid and the QDs are initially imaged by wide-field microscopy
53 with the camera in a single acquisition (6s), as shown in Figure 1(b) in gray-scale. By
54 reflecting the 1550 nm LED light, the gold metal strips are distinct from the InGaAs
55 surface, despite being approximately 40% darker. This effect is due to the background
56
57
58
59
60

PL emission of our sample [41], whose intensity is comparable to that of the reflected 1550 nm light. The choice of LED intensity and integration time is a compromise between three desirable features of the image: the grid imaged by reflection with a good contrast, the PL signal of the QDs [33] not masked by the reflected signal and the pixels not being saturated. With the current configuration found as optimal, the signal of the QDs is larger than that of the InGaAs surface by factor between 1.3 and 2, depending on the brightness of the QD. A larger contrast could in principle be achieved by imaging a sample without background emission in the spectral range of interest. The edges of the grid exhibit a slight blurring due to the large diffraction-limited spot size and are clearly discernible by an intensity dip caused by scattering, which is a beneficial feature for localization. Specifically, the inner of the metal strips and the InGaAs surface are brighter than the edges by factors of about 1.3 and 2.1, respectively. The noise level of the camera constitutes 1% of the grayscale, resulting in a PL signal to camera noise around 10 for QDs with an average brightness. At this level, the emitters can be localized with good accuracy [36]. To get more insight on the spectral properties of QDs detected by the camera, PL spectra can be acquired by locally exciting with the laser and measuring the dispersed PL signal with the PDA, as shown in Figure 1(c). As a consequence of the high density of QDs, the spectra consist of numerous lines originating from multiple QDs excited within the laser spot area. Therefore, the majority of the spots captured by the camera likely stem from clusters of QDs rather than individual ones, even when employing the 12 nm bandwidth filter. In principle, this effect can be mitigated by reducing the bandwidth of the filter to 1 or 2 nm. However, the signal-to-noise ratio will decrease to the extent that individual emitters can no longer be localized efficiently. We note that a more sophisticated camera with a better cooling system to lower the noise level may alleviate this issue, but imaging dim emitters will remain challenging.

An image of the same unit cell was also obtained by confocal laser scanning microscopy. The signal was recorded with the spectrometer and the liquid nitrogen-cooled InGaAs PDA. At each step, PL spectra were recorded with a 55 pm wavelength resolution within a 28 nm range. Despite the longer acquisition time (7h for a 160x160 pixels image), the emission wavelength and the position of the QDs can be simultaneously recorded. Figure 1(d) depicts only the QDs emitting at 1551.6nm which are well-isolated by the narrow filtering. The lineshape can also be investigated from the PL spectra, as shown in Figure 1(c). The QD "A" exhibits the desirable sharp and isolated emission line and previous studies [27, 33] on the same type of QDs demonstrated that it can be a promising single photon source. The emission lines of the other labeled QDs are broader and may overlap with adjacent lines, which would likely not be considered for integration. With the chosen intensity of the LED signal, the intensity of the reflected light on InGaAs surface is larger by a factor of about 5.8 than that measured at the edges of the marker. Similarly, this factor is about 4.9 between the inner part of the markers and their edges. With the background level

of the camera being as low as 50 counts/s, the QD can be detected with a signal-to-noise ratio around 150. Since the count rate is below saturation (6.5×10^4 counts/s), the LED intensity could be increased further to enhance the contrast between the grid and the surface without compromising the contrast between the QDs and the surface. The better performances in terms of spectral filtering while achieving a higher contrast and significantly larger signal-to-noise ratio demonstrate the viability of the scanning approach to localize telecom QDs.

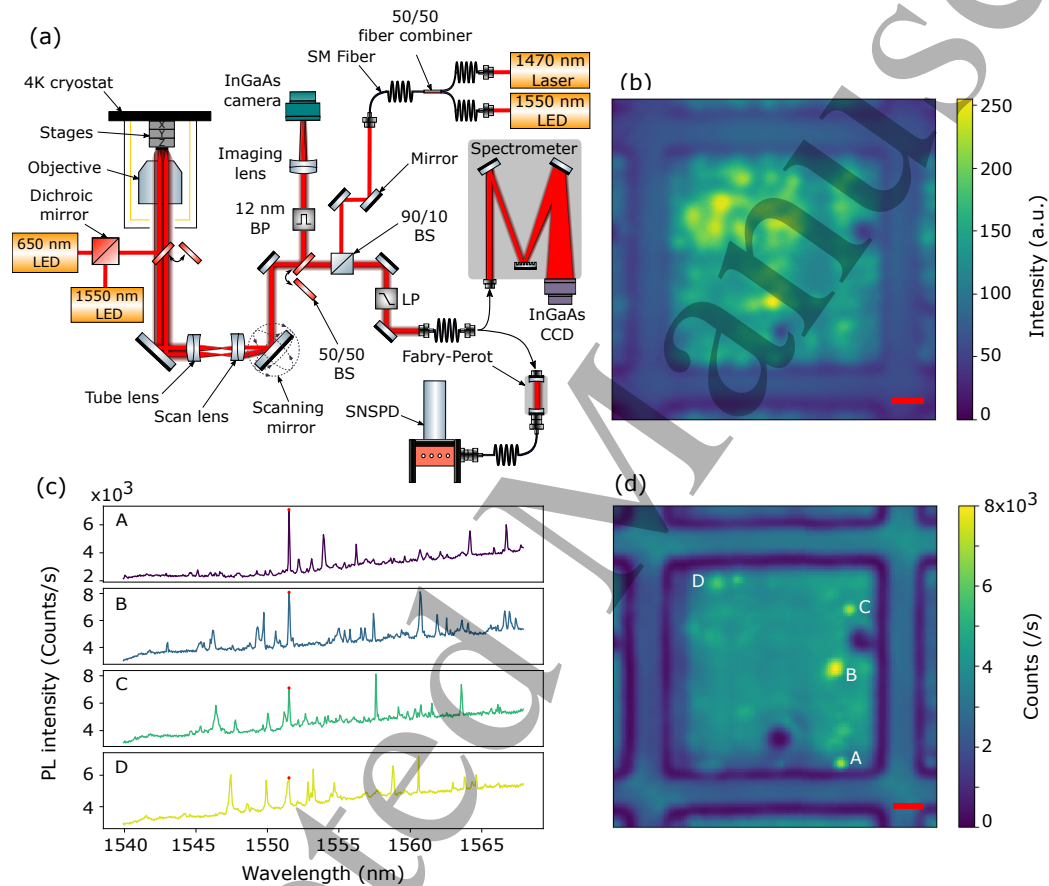


Figure 1. (a) Sketch of the confocal laser scanning microscope and wide-field imaging system. (b) Wide-field PL image of the sample after filtering with a (1550 ± 6) nm bandpass. The exposure time was set to 6s. The two dark spots on the image correspond to two metal markers used to label the unit cell. (c) Four PL spectra showing the emission line (red dot) of the QDs emitting at 1551.6 nm and labeled A, B, C and D in (d). The QDs were excited by the laser and the signal recorded with the InGaAs PDA consists of the diffracted PL signal together with reflected light incoherent light. (d) PL map at 1551.6 nm of the previous unit cell obtained by scanning and by recording the diffracted signal with the InGaAs sensor. For the two images, the scale bar is $3 \mu\text{m}$ and distortions have been corrected.

3.2. Procedure to locate the QDs

To detail our methodology for QD localization, we consider one unit-cell as shown by the scanning electron microscopy (SEM) image in Figure 2(a). The patterned EBL grid

1
2
3
4
5 does not exhibit discernible deformations that could have occurred during writing, as
6 confirmed by inspection under the SEM. Henceforth, we proceed with the assumption
7 that the imaged grids match the EBL pattern file. A high-resolution grayscale PL
8 scan (390x390 pixels, corresponding to angular steps of 0.0023°) of this unit cell was
9 acquired, as shown in Figure 2(b). The signal was filtered at (1550 ± 0.5) nm with
10 a fiber Fabry-Perot and detected with an SNSPD. Photons were counted for 100 ms
11 by the built-in driver of the detector and recorded by the control computer at each
12 scanning step (communication delay of 150 ms). Compared to the previous detection
13 method with the spectrometer, the scanning speed is increased by a factor of five and the
14 narrow filtering still allows for the identification of QDs with non-overlapping emission
15 profiles. However, the contrast between the metal strips and the surface is insufficient
16 to accurately identify the edges. Therefore, the power of the LED signal at 1550 nm
17 was increased, as shown in Figure 2(c). The QDs remain easily discernible above the
18 reflected light background. The morphology of the surface, characterized by a cross-
19 hatch pattern typical of heterostructure with a MMB [42, 43], also becomes apparent.
20 Some faint shadows of edges can be seen due to instrument aberrations, but this artifact
21 does not affect the image analysis. The horizontal line-cut (Figure 2(e)) reveals that the
22 edges of the strip are darker by at least a factor 3 and 5 compared to the inner section
23 of strip and the InGaAs surface, respectively. Despite the reflected background, the
24 amplitude of the QDs highlighted still represents between 15 and 23 % of the grayscale
25 intensity of the map.
26
27
28
29
30
31
32
33
34
35
36
37
38
39
40
41
42
43
44
45
46
47
48
49
50
51
52
53
54
55
56
57
58
59
60

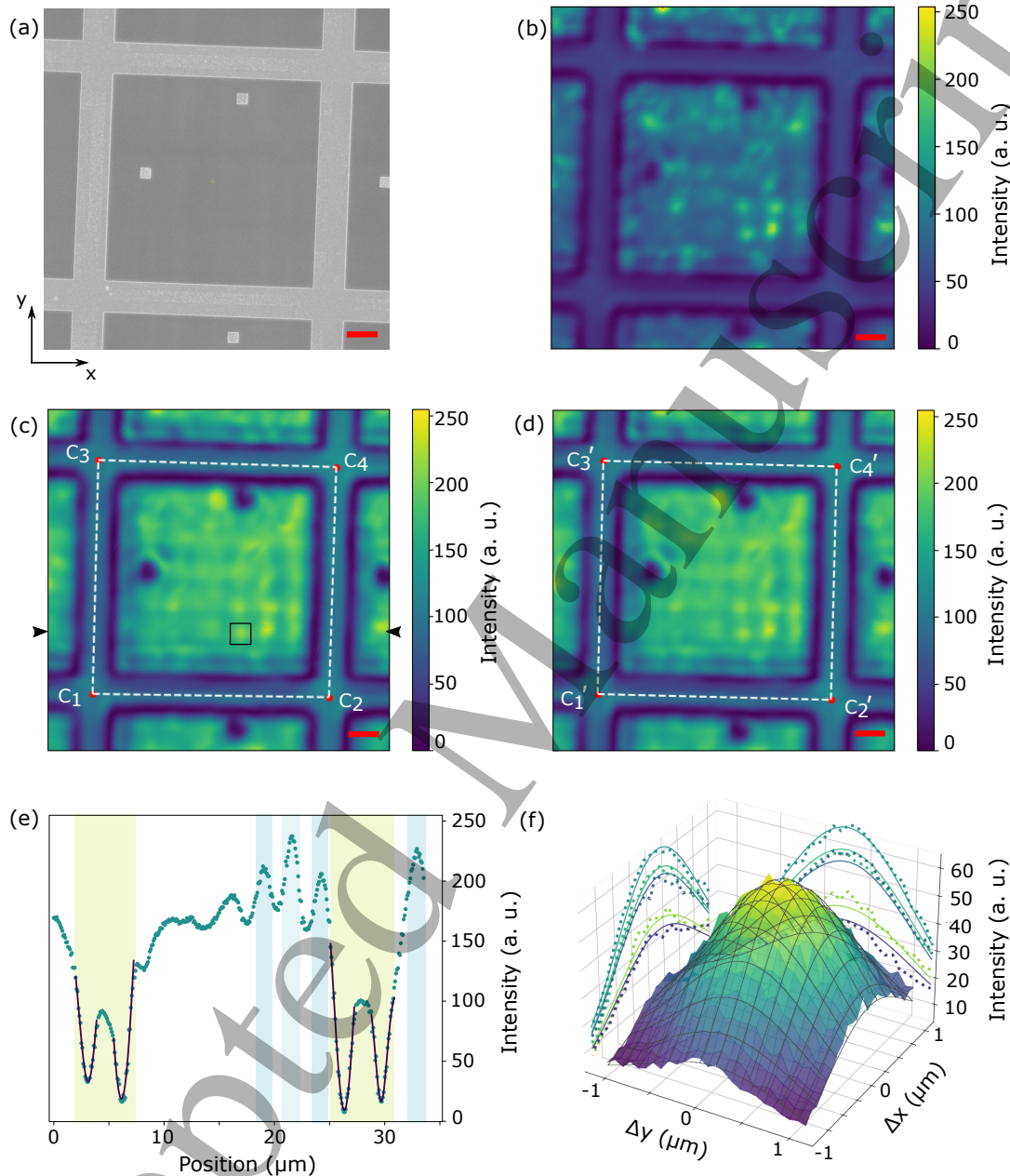


Figure 2. (a) SEM image of the investigated unit cell. The scale bar is $3 \mu\text{m}$ for the SEM image and the PL maps. (b) Grayscale PL image acquired by scanning and recording the signal with a fiber Fabry-Perot and an SNSPD. The whole acquisition took 10.5h. (c) Same PL map acquired with more incoherent light at 1550 nm to enhance the reflected signal on the metal strips. The dashed white lines indicate the center of the metal strips obtained after edge detection. The pixel size is 86.2 nm, calculated from the distance between the corners C_1 and C_3 . (d) PL map after perspective transform correction. (e) Horizontal line-cut at the position indicated by the two arrows in the map. The green and blue regions highlight the metal strips and bright QDs, respectively. The edges of the metal strip are found by gaussian fitting. (f) Fitting of the QD indicated by the black square in (c) by an elliptical gaussian distribution. The FWHM are $\approx 732.8 \text{ nm}$ and $\approx 659.6 \text{ nm}$ along the x-axis and y-axis, respectively.

The strategy to locate the QDs consists in first finding the four inner and outer edges of the grid with multiple horizontal or vertical line-cuts. For each of them, the minimum of the intensity dip at the edge is fit with a gaussian function with the least-squares method. The FWHM of the fitted profile is on average 940 nm for the four edges in the line-cut shown in Figure 2(e). The middle distance between the inner and outer edges is then linearly fitted with a slope s_i and intercept r_i by least-squares method ($i=1,\dots,4$ for the four strips). The curved edges near the crosses are avoided for better accuracy. The intersections of the four lines provide the four corners of the grid $\mathbf{C}_i = (C_{i,x}, C_{i,y})$, forming a basis to locate the QDs. Finally, the QD centers are found by fitting their emission profile with an elliptical gaussian function, as depicted in Figure 2(f). For a QD with average brightness, boxed in Figure 2(c), the fitting standard error on the position of the center is $\sigma_{QD,x} = 3.6$ nm and $\sigma_{QD,y} = 3.3$ nm ($\sigma_{QD} = \sqrt{(\sigma_{QD,x})^2 + (\sigma_{QD,y})^2} = 4.8$ nm).

A close inspection of the scanned PL map reveals a distortion of the detected grid, stemming from aberrations introduced by the imaging system. Typically resulting from a combination of multiple causes such as imperfect alignment, placement and specifications of the optical components, the aberrations can be minimized but never completely eliminated. A shearing, an elongation or a combination of both in the image could also originate from a linear drift of the sample inside the cryostat during acquisition. However, we could repeat the same deformation as observed in Figure 2(c) by running a faster map, which indicates that it is primarily introduced by the scanner. These distortions modify the positions of the corners and the QDs on the map and have to be corrected to obtain accurate coordinates.

In our correction process, we consider both linear transformations (rotation, scaling, shearing and translation) and non-orthogonal transformations (perspective) [44]. Given the small angles scanned by the mirror and therefore the scan field of view, we approximate higher order effects like barrel and pin-cushion to a perspective deformation on the scale of the acquired map. For each point of the map, the corrected coordinates $\mathbf{X}' = (x', y')$ are found from the 3x3 perspective matrix \mathbf{P} and the distorted coordinates $\mathbf{X} = (x, y)$ as:

$$\begin{pmatrix} tx' \\ ty' \\ t \end{pmatrix} = \begin{pmatrix} a_1 & a_2 & a_3 \\ a_4 & a_5 & a_6 \\ a_7 & a_8 & 1 \end{pmatrix} \begin{pmatrix} x \\ y \\ 1 \end{pmatrix}. \quad (1)$$

The coefficients of the matrix \mathbf{P} are derived by solving the system of 8 equations, which maps the coordinates of the four distorted corners \mathbf{C}_i to the corners \mathbf{C}'_i of an ideal unit cell. To construct the latter, we choose the two corners found with the smallest error as invariant (C_1 and C_3), while the other two are geometrically constructed. Other constructions are possible: the resulting map would then differ by a rotation and scaling factor, but the QD position after correction would remain the same in the reference frame of the corrected corners. While identifying four corners in the distorted map is required to define the perspective transformation, finding the distance of the QD with respect

to two corrected corners is sufficient to know its position, and knowing its distance to the two other corners will not enhance the accuracy. Figure 2(d) shows the PL map after correction, and the disparities with the uncorrected map are hardly noticeable. The QD positions are corrected by applying the perspective transform (eq. 1) to the distorted coordinates as found in Figure 2(f). In this case, the QD corrected position lies 298.0 nm and 53.7 nm away from its originally found position, in the x- and y-directions respectively, which corresponds to a total distance of 302.8 nm. Compared to photonic structures typically on the scale of 1 to 2 μm , these values are significant and thus emphasize the need for correcting the distortions in order to obtain a good alignment.

3.3. Uncertainty on the position

For each of the four lines fitting the middle of the four strips, we write $\sigma_{s,i}$ and $\sigma_{r,i}$ the fitting standard errors of the slope and intercept, respectively. Since the lines were detected separately and away from the corners, the uncertainties on the slopes and intercepts are uncorrelated. The coordinates of the corners \mathbf{C}_i are found by solving the linear system of two intersecting lines, and we write $\sigma_{C_i} = (\sigma_{C_{i,x}}, \sigma_{C_{i,y}})$ the uncertainty on their positions. By error propagation, they are expressed as:

$$\sigma_{C_{i,x}} = \sqrt{\sum_n \left[\left(\frac{\partial C_{i,x}}{\partial s_n} \sigma_{s,n} \right)^2 + \left(\frac{\partial C_{i,x}}{\partial r_n} \sigma_{r,n} \right)^2 \right]}, \quad (2)$$

where n corresponds to the index of the two lines used to find the corner \mathbf{C}_i . A similar expression is found for the y-coordinate of the corners. The full form equations are derived analytically with Wolfram Mathematica and the numerical values can be subsequently computed. We define the error on the position of the corner as $\sigma_{C_i} = \sqrt{(\sigma_{C_{i,x}})^2 + (\sigma_{C_{i,y}})^2}$, which lays between 13.2 nm and 56.8 nm depending on the corner. Without correcting the distortion, the error on the position of the QD with respect to one of the corners [40] is then $\sigma_{QD+C_i} = \sqrt{(\sigma_{QD})^2 + (\sigma_{C_i})^2}$, which is equal to 14.0 nm by choosing the corner C_3 found with the smallest error.

By correcting the distortion of the image, the error on the position of the distorted corners \mathbf{C}_i must be propagated to the perspective transform \mathbf{P} . The positions of the destination corners \mathbf{C}'_i are by definition ideal and do not bear any error. The uncertainty of the coefficients a_i is then calculated by:

$$\sigma_{a_i} = \sqrt{\sum_{i=1}^4 \left[\left(\frac{\partial a_i}{\partial C_{i,x}} \sigma_{C_{i,x}} \right)^2 + \left(\frac{\partial a_i}{\partial C_{i,y}} \sigma_{C_{i,y}} \right)^2 \right]}. \quad (3)$$

Finally, the uncertainty $\sigma'_X = (\sigma_{x'}, \sigma_{y'})$ on the corrected position \mathbf{X}' of each point of the map is given by:

$$\sigma_{x'} = \sqrt{\sum_{i=1}^8 \left[\left(\frac{\partial x'}{\partial a_i} \sigma_{a_i} \right)^2 \right] + \left(\frac{\partial x'}{\partial x} \sigma_x \right)^2 + \left(\frac{\partial x'}{\partial y} \sigma_y \right)^2}, \quad (4)$$

where $\sigma_X = (\sigma_x, \sigma_y)$ is the uncertainty of the location of a point in the distorted map. A similar equation is found for $\sigma_{y'}$. The propagation of errors for the QD located in Figure 2(c) gives $\sigma_{QD,x'} = 123.4$ nm and $\sigma_{QD,y'} = 93.8$ nm ($\sigma_{QD'} = \sqrt{(\sigma_{QD,x'})^2 + (\sigma_{QD,y'})^2} = 155.0$ nm and $\sigma_{QD'} = \sigma_{QD'+C'_3}$ since there is no error in the position of C'_3). These values, significantly larger than that obtained before corrections, show that the distortion is the dominant source of errors in our mapping technique. To contextualize these errors, we simulated by Finite-Difference Time-Domain (Figure 3(a)) the enhancement in collection efficiency at 1550 nm provided by etching a pillar (diameter 2.3 μ m and height 500 nm) in our sample. A perfectly aligned QD with the center of the pillar results in a 23% collection efficiency by the microscope objective. As illustrated in Figure 3(b), the design proves resilient to a misalignment below 80 nm which lays within the capabilities of our scanner in the absence of distortions, but a shift of around 155 nm would degrade the performance down to 14%.

4. Discussion

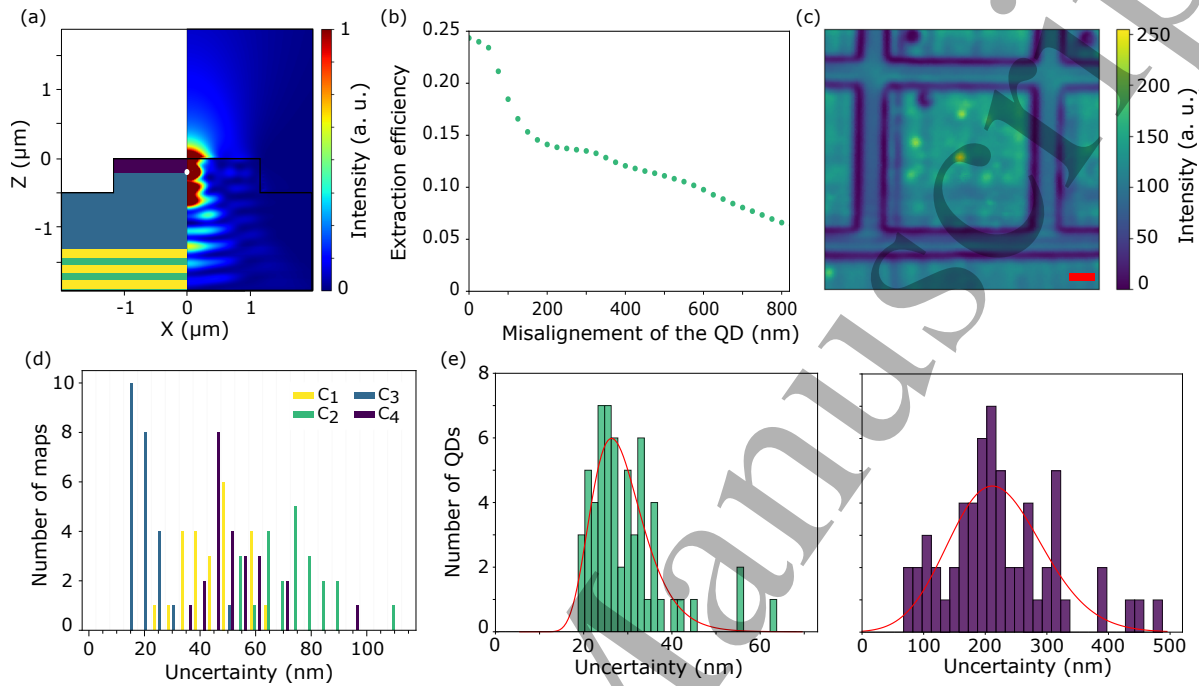


Figure 3. (a) Electric field intensity (E^2) profile of a pillar etched (diameter $2.3 \mu\text{m}$ and height 500 nm) in the sample (purple: capping layer, blue: metamorphic buffer, yellow: AlAs, Green: GaAs). (b) Influence of the misalignment QD/pillar on the collection efficiency. (c) Example of a 240×230 pixels grayscale PL image as acquired. The scale bar is $3 \mu\text{m}$. (d) Histogram of the errors on the location of the four corners. The orientation of all maps remains consistent, with the labeling of the four corners following the convention established in Figure 2. (e) Histogram of the error on the QDs position located in the 24 grids before (left) and after (right) correction of distortions, fitted by a log-normal distribution (red line).

In contrast to previous studies employing wide-field imaging, our confocal laser scanner can provide the PL spectra of the mapped QDs, allowing to spatially and spectrally couple them to fabricated photonic structures. To compare our alignment accuracy, and specifically with emitters at 1550 nm , we note that an uncertainty below 80 nm for 10 % of the emitters has been demonstrated with wide-field imaging [36]. Our mapping technique reaches an even lower level, assuming a perfectly aligned scanner. Yet, we find that the correction of distortions, even visually imperceptible, can significantly increase the final uncertainty by error propagation. An even more precise adjustment of our instrument will noticeably help to minimize distortions. We also conducted a more in-depth analysis of the effects of distortions which are, to the best of our knowledge, neglected in earlier works. For QDs emitting below $1 \mu\text{m}$, marker-based PL imaging locates the QDs with uncertainties below 10 nm , but offsets between the QD and the fabricated photonic structure are often measured up to 100 nm even after subtraction of the error introduced by EBL [40]. The quality of the marker and the fitting method

1
2
3
4
5 may contribute to this discrepancy, but a deformation of the whole image such as a
6 perspective or a barrel/pin-cushion could also have an impact at such a small scale.
7 The better performance of in-situ EBL [26], where the photonic structure is directly
8 fabricated on the QD without the need of marker-based positioning, also hints towards
9 detrimental effects of distortions.
10

11 To demonstrate the repeatability of both the mapping and the analysis approach
12 described above, QDs were located over 24 unit cells distributed across the chip. The
13 angular stepsize was changed to 0.0040° for faster acquisition of 240×230 pixels PL maps,
14 as shown in Figure 3(c). A degradation of the positioning accuracy compared to the
15 higher resolution map in Figure 2(c) is therefore expected due to the larger pixel size,
16 but this does not influence the positioning error distribution. The histogram of the error
17 σ_{C_i} on the position of the four corners (Figure 3(d)) indicates that the mean error varies
18 with the corner fitted, from 22.8 nm for the top left corner to 78.0 nm for the bottom
19 right corner. This systematic difference can be attributed to a change of contrast at the
20 edges of the metal strips, possibly due to a tilt of the sample. On this set of PL maps,
21 QDs were located prior to any processing, and then mapped to their distortion-free
22 positions. On average, we obtain a shift in their position of 427.9 nm, underscoring the
23 importance of the distortion correction procedure. Figure 3(e) depicts the distribution
24 of the uncertainty on their position σ_{QD+C_3} and $\sigma_{QD'}$ before and after the distortion
25 correction, respectively. The uncertainty profiles can be best fitted with a log-normal
26 distribution, and we obtain a median error of 27.9 nm and 216.5 nm, respectively. We
27 find that 10% of the QDs have an uncertainty below 11 nm and 110 nm, respectively.
28 The spread of the uncertainty distributions can stem from various factors, including the
29 proximity of the surface to the focal plane of the objective, the brightness of the QD,
30 the severity of the distortion at the QD location or the presence of weak neighboring
31 emitters affecting the spatial profile.
32
33

34 We expect that a better positioning accuracy of the scanner can be obtained by
35 imaging a sample without any background emission at telecom wavelength, as well as
36 by improving the alignment accuracy which would reduce the amount of distortions.
37 Indeed, the scanning mirror could be mounted on translation stages to ensure that the
38 optical beams impinge on its center in order to avoid geometric distortions. Similarly,
39 the scan and tube lenses could also be mounted on translation stages to improve the 4-f
40 system. If space allows, increasing the focal lengths of the lenses and thus increasing
41 their radii of curvature would minimize spherical aberrations. Finally, a perspective
42 effect can occur if the sample plane is not perpendicular to the optical axis of the
43 objective. This could be compensated for by inserting tilting stages on top of the xyz
44 stack in the cryostat.
45

46 Further improvements of the scanning microscope can be envisioned. Pumping
47 the QDs above-band within the achromatic range of the optics would reduce the laser
48 excitation spot size, thereby decreasing the lateral size of the QDs in the images. This
49 reduction could potentially minimize the overlap between neighboring QDs and enhance
50 the fitting accuracy. In terms of scanning speed, the photon counts could be continuously
51
52
53
54
55
56
57
58
59
60

recorded along with trigger signals generated by the scanning mirror at each step by a fast counting card. The resulting PL map would only be retrieved at the end of the acquisition. This scheme would suppress the communication delay at each step, reducing the acquisition time of the PL maps presented above by a factor 2.5, increasing the throughput of our system. This reduction would also be advantageous since the map acquisition would become more robust against potential sample drift. Thereafter, the reflected signal around 1550 nm used for marker identification could be separated from the PL signal of the sample by a narrow-band notch filter at the emission wavelength of interest of the QDs and placed after the longpass filter. In this configuration, one avalanche photodiode or SNSPD would detect the reflected signal while another one would detect the PL signal further filtered by the Fabry Perot at a wavelength inside of the notch filter bandwidth. With such a setup, the intensity of the 1550 nm LED used to image to the metal strips can be increased without raising the overall background of the map.

5. Conclusion

In conclusion, we used confocal laser scanning microscopy for both spatial localization and spectral characterization of QDs emitting in the telecom C-band. This approach isolates and locates dense and dim emitters within a narrow spectral bandwidth, with a better contrast and signal-to-noise ratio than the wide-field imaging technique. Our method demonstrates an alignment uncertainty below 11 nm for 240x230 pixel maps for 10% of the QDs, in the absence of distortions of the image. Yet, we found that the QD positions in the as-acquired PL maps were shifted by 428 nm on average compared to their corrected positions due to optical distortions in our system. After distortion correction and error propagation, the final uncertainty increases to 110 nm. This non-negligible shift underlines the need to consider the detrimental effects of distortions for accurate positioning, given their unavoidable occurrence in any optical system. Fabrication of photonic structures such as micro-pillars and micro-lenses which tolerate our current alignment error is already possible with our scanner capabilities. We anticipate that an even finer alignment to reduce aberrations of the system will enhance the final accuracy, enabling fabrication of more sophisticated devices based on photonic cavities or circular Bragg gratings.

6. Author contributions

Conceptualization, T.D. and V.Z.; methodology, T.D. and A.B.; formal analysis, T.D., A.B and M.Huet; investigation, T.D., A.B and M.Huet; resources, M.Hammar.; data curation, T.D., A.B., M.Huet; writing—original draft preparation, T.D.; writing—review and editing, T.D., A.B, M.Huet, M.Hammar and V.Z.; supervision, T.D. and V.Z.; funding acquisition, V.Z.

7. Acknowledgements

This research was funded by the Swedish Research Council (VR) grants (reference 2023-04604 ; 2023-05663 ; 2020-04861).

8. Data availability statement

The data that support the findings of this study are available upon reasonable request from the authors.

References

- [1] Basset F B, Valeri M, Rocchia E, Muredda V, Poderini D, Neuwirth J, Spagnolo N, Rota M B, Carvacho G, Sciarrino F and Trotta R 2021 *Science Advances* **7** 6379 ISSN 23752548 (*Preprint* 2007.12727)
- [2] Zhai L, Nguyen G N, Spinnler C, Ritzmann J, Löbl M C, Wieck A D, Ludwig A, Javadi A and Warburton R J 2022 *Nature Nanotechnology* **17** 829–833 ISSN 17483395 (*Preprint* 2106.03871)
- [3] Heindel T, Kim J H, Gregersen N, Rastelli A and Reitzenstein S 2023 *Advances in Optics and Photonics* **15** 613 ISSN 1943-8206 (*Preprint* 2309.04229)
- [4] Moody G, Sorger V J, Blumenthal D J, Juodawlkis P W, Loh W, Sorace-Agaskar C, Jones A E, Balram K C, Matthews J C, Laing A, Davanco M, Chang L, Bowers J E, Quack N, Galland C, Aharonovich I, Wolff M A, Schuck C, Sinclair N, Lončar M, Komljenovic T, Weld D, Mookherjea S, Buckley S, Radulaski M, Reitzenstein S, Pingault B, Machielse B, Mukhopadhyay D, Akimov A, Zheltikov A, Agarwal G S, Srinivasan K, Lu J, Tang H X, Jiang W, McKenna T P, Safavi-Naeini A H, Steinhauer S, Elshaari A W, Zwiller V, Davids P S, Martinez N, Gehl M, Chiaverini J, Mehta K K, Romero J, Lingaraju N B, Weiner A M, Peace D, Cernansky R, Lobino M, Diamanti E, Vidarte L T and Camacho R M 2022 *JPhys Photonics* **4** 012501 ISSN 25157647
- [5] Castelletto S and Boretti A 2023 *Advanced Quantum Technologies* **6** 2300145 ISSN 25119044
- [6] Schweickert L, Jöns K D, Zeuner K D, Covre Da Silva S F, Huang H, Lettner T, Reindl M, Zichi J, Trotta R, Rastelli A and Zwiller V 2018 *Applied Physics Letters* **112** 93106 ISSN 00036951 (*Preprint* 1712.06937)
- [7] Schöll E, Hanschke L, Schweickert L, Zeuner K D, Reindl M, Covre Da Silva S F, Lettner T, Trotta R, Finley J J, Müller K, Rastelli A, Zwiller V and Jöns K D 2019 *Nano Letters* **19** 2404–2410 ISSN 15306992 (*Preprint* 1901.09721) URL <https://pubs.acs.org/sharingguidelines>
- [8] Müller T, Skiba-Szymanska J, Krysa A B, Huwer J, Felle M, Anderson M, Stevenson R M, Heffernan J, Ritchie D A and Shields A J 2018 *Nature Communications* **2018 9:1** 9 1–6 ISSN 2041-1723 (*Preprint* 1710.03639)
- [9] Yu Y, Liu S, Lee C M, Michler P, Reitzenstein S, Srinivasan K, Waks E and Liu J 2023 *Nature Nanotechnology* **18** 1389–1400 ISSN 17483395 (*Preprint* 2311.03993)
- [10] Hepp S, Jetter M, Portalupi S L and Michler P 2019 *Advanced Quantum Technologies* **2** 1900020 ISSN 2511-9044
- [11] Carter S G, Sweeney T M, Kim M, Kim C S, Solenov D, Economou S E, Reinecke T L, Yang L, Bracker A S and Gammon D 2013 *Nature Photonics* **7** 329–334 ISSN 17494885 (*Preprint* 1211.4540)
- [12] Wang H, He Y M, Chung T H, Hu H, Yu Y, Chen S, Ding X, Chen M C, Qin J, Yang X, Liu R Z, Duan Z C, Li J P, Gerhardt S, Winkler K, Jurkat J, Wang L J, Gregersen N, Huo Y H, Dai Q, Yu S, Höfling S, Lu C Y and Pan J W 2019 *Nature Photonics* **13** 770–775 ISSN 17494893
- [13] Doughty G, Thoms S, Law V and Wilkinson C 1986 *Vacuum* **36** 803–806 ISSN 0042-207X
- [14] Varoutsis S, Laurent S, Laurent S, Sagnes I, Lemaître A, Ferlazzo L, Mériadec C, Patriarche G, Robert-Philip I and Abram I 2005 *Journal of Vacuum Science & Technology B: Microelectronics*

- and Nanometer Structures Processing, Measurement, and Phenomena **23** 2499–2503 ISSN 1071-1023
- [15] Krieger T M, Weidinger C, Oberleitner T, Undeutsch G, Rota M B, Tajik N, Aigner M, Buchinger Q, Schimpf C, Garcia A J, Covre da Silva S F, Höfling S, Huber-Loyola T, Trotta R and Rastelli A 2024 *ACS Photonics* **11** 596–603 ISSN 23304022 (*Preprint* 2309.15801)
- [16] Albert F, Sivalertporn K, Kasprzak J, Strauß M, Schneider C, Höfling S, Kamp M, Forchel A, Reitzenstein S, Muljarov E A and Langbein W 2013 *Nature Communications* **4** 1–6 ISSN 20411723
- [17] Liu J, Konthasinghe K, Davanço M, Lawall J, Anant V, Verma V, Mirin R, Nam S W, Song J D, Ma B, Chen Z S, Ni H Q, Niu Z C and Srinivasan K 2018 *Physical Review Applied* **9** 064019 ISSN 23317019
- [18] Dalgarno P A, Smith J M, McFarlane J, Gerardot B D, Karrai K, Badolato A, Petroff P M and Warburton R J 2008 *Physical Review B - Condensed Matter and Materials Physics* **77** 245311 ISSN 10980121
- [19] Warburton R J 2013 *Nature Materials* **12** 483–493 ISSN 14764660
- [20] Sautter K E, Vallejo K D and Simmonds P J 2020 *Journal of Applied Physics* **128** ISSN 10897550
- [21] Sutula M, Christen I, Bersin E, Walsh M P, Chen K C, Mallek J, Melville A, Titze M, Bielejec E S, Hamilton S, Braje D, Dixon P B and Englund D R 2023 *Nature Materials* **22** 1338–1344 ISSN 14764660 (*Preprint* 2210.13643)
- [22] Liu J, Davanço M I, Sapienza L, Konthasinghe K, De Miranda Cardoso J V, Song J D, Badolato A and Srinivasan K 2017 *Review of Scientific Instruments* **88** 023116 ISSN 10897623 (*Preprint* 1612.07412)
- [23] Liu S, Li X, Liu H, Qiu G, Ma J, Nie L, Ni H, Niu Z, Qiu C W, Wang X and Liu J 2023 (*Preprint* 2311.02626) URL <http://arxiv.org/abs/2311.02626>
- [24] Thon S M, Rakher M T, Kim H, Gudat J, Irvine W T, Petroff P M and Bouwmeester D 2009 *Applied Physics Letters* **94** 111115 ISSN 00036951
- [25] Dousse A, Lanco L, Suffczyński J, Semenova E, Miard A, Lemaître A, Sagnes I, Roblin C, Bloch J and Senellart P 2008 *Physical Review Letters* **101** 267404 ISSN 00319007 (*Preprint* 0807.4427)
- [26] Rodt S and Reitzenstein S 2021 *Nano Express* **2** 014007 ISSN 2632959X
- [27] Zeuner K D, Paul M, Lettner T, Reuterskiöld Hedlund C, Schweickert L, Steinhauer S, Yang L, Zichi J, Hammar M, Jöns K D and Zwiller V 2018 *Applied Physics Letters* **112** 173102 ISSN 00036951 (*Preprint* 1801.01518)
- [28] Vajner D A, Holewa P, Zięba-Ostój E, Wasiluk M, von Helversen M, Sakanas A, Huck A, Yvind K, Gregersen N, Musiał A, Syperek M, Semenova E and Heindel T 2024 *ACS Photonics* **11** 339–347 ISSN 23304022 (*Preprint* 2306.08668)
- [29] Huo Y H, Rastelli A and Schmidt O G 2013 *Applied Physics Letters* **102** 152105 ISSN 00036951 URL <https://doi.org/10.1063/1.4802088>
- [30] Huber D, Reindl M, Aberl J, Rastelli A and Trotta R 2018 *Journal of Optics (United Kingdom)* **20** ISSN 20408986 (*Preprint* 1804.10472)
- [31] Nawrath C, Joos R, Kolatschek S, Bauer S, Pruy P, Hornung F, Fischer J, Huang J, Vijayan P, Sittig R, Jetter M, Portalupi S L and Michler P 2023 *Advanced Quantum Technologies* **6** 2300111 ISSN 2511-9044
- [32] Holewa P, Sakanas A, Gür U M, Mrowiński P, Huck A, Wang B Y, Musiał A, Yvind K, Gregersen N, Syperek M and Semenova E 2022 *ACS Photonics* **9** 2273–2279 ISSN 23304022 (*Preprint* 2104.07589)
- [33] Zeuner K D, Jöns K D, Schweickert L, Reuterskiöld Hedlund C, Nuñez Lobato C, Lettner T, Wang K, Gyger S, Schöll E, Steinhauer S, Hammar M and Zwiller V 2021 *ACS Photonics* **8** 2337–2344 ISSN 23304022
- [34] Reindl M, Jöns K D, Huber D, Schimpf C, Huo Y, Zwiller V, Rastelli A and Trotta R 2017 *Nano Letters* **17** 4090–4095 ISSN 15306992 (*Preprint* 1701.07812)
- [35] Chen Y, Spinelli S and Pan Z 2024 *Journal of Materials Chemistry C* ISSN 2050-7526

- 1
2
3
4
5 [36] Holewa P, Zięba-Ostój E, Vajner D A, Wasiluk M, Gaál B, Sakanas A, Burakowski M, Mrowiński
6 P, Krajnik B, Xiong M, Huck A, Yvind K, Gregersen N, Musiał A, Heindel T, Syperek M and
7 Semenova E 2023 *Nature Communications* **15** 1–9 ISSN 2041-1723 (*Preprint* 2304.02515)
- 8 [37] Yan, Chunze and Shi, Yusheng and Zhaoqing, Li and Wen, Shifeng and Wei Q 2020 *Selective Laser*
9 *Sintering Additive Manufacturing Technology* (San Diego, CA: Academic Press)
- 10 [38] Pedrotti, Frank L and Pedrotti, Leno M and Pedrotti L S 2017 *Introduction to Optics* 3rd ed
11 (Cambridge: Cambridge University Press)
- 12 [39] Sapienza L, Davanço M, Badolato A and Srinivasan K 2015 *Nature Communications* **6** 1–8 ISSN
13 20411723 (*Preprint* 1503.07141)
- 14 [40] Madigawa A A, Donges J N, Gaál B, Li S, Liu H, Dai D, Su X, Shang X, Ni H, Schall J, Rodt
15 S, Niu Z, Gregersen N, Reitzenstein S and Munkhbat B 2023 *ACS Photonics* ISSN 2330-4022
16 (*Preprint* 2309.14795)
- 17 [41] Paul M, Olbrich F, Höschele J, Schreier S, Kettler J, Portalupi S L, Jetter M and Michler P 2017
18 *Applied Physics Letters* **111** 33102 ISSN 00036951
- 19 [42] Sittig R, Nawrath C, Kolatschek S, Bauer S, Schaber R, Huang J, Vijayan P, Pruy P, Portalupi
20 S L, Jetter M and Michler P 2022 *Nanophotonics* **11** 1109–1116 ISSN 21928614 (*Preprint*
21 2107.13371)
- 22 [43] Andrews A M, Speck J S, Romanov A E, Bobeth M and Pompe W 2002 *Journal of Applied Physics*
23 **91** 1933–1943 ISSN 00218979
- 24 [44] Zeng Z 2022 *Towards an optical interface to spin qubits* Ph.D. thesis RWTH Aachen University
25
26
27
28
29
30
31
32
33
34
35
36
37
38
39
40
41
42
43
44
45
46
47
48
49
50
51
52
53
54
55
56
57
58
59
60